



CHORUS

This is the accepted manuscript made available via CHORUS. The article has been published as:

Gravitational wave content and stability of uniformly, rotating, triaxial neutron stars in general relativity

Antonios Tsokaros, Milton Ruiz, Vasileios Paschalidis, Stuart L. Shapiro, Luca Baiotti, and Kōji Uryū

Phys. Rev. D **95**, 124057 — Published 30 June 2017

DOI: [10.1103/PhysRevD.95.124057](https://doi.org/10.1103/PhysRevD.95.124057)

Gravitational wave content and stability of uniformly, rotating, triaxial neutron stars in general relativity.

Antonios Tsokaros,¹ Milton Ruiz,¹ Vasileios Paschalidis,² Stuart L. Shapiro,^{1,3} Luca Baiotti,⁴ and Kōji Uryū⁵

¹*Department of Physics, University of Illinois at Urbana-Champaign, Urbana, IL 61801*

²*Department of Physics, Princeton University, Princeton, NJ 08544*

³*Department of Astronomy & NCSA, University of Illinois at Urbana-Champaign, Urbana, IL 61801*

⁴*Graduate School of Science, Osaka University, 560-0043 Toyonaka, Japan*

⁵*Department of Physics, University of the Ryukyus, Senbaru, Nishihara, Okinawa 903-0213, Japan*

(Dated: May 23, 2017)

Targets for ground-based gravitational wave interferometers include continuous, quasi-periodic sources of gravitational radiation, such as isolated, spinning neutron stars. In this work we perform evolution simulations of uniformly rotating, triaxially deformed stars, the compressible analogues in general relativity of incompressible, Newtonian Jacobi ellipsoids. We investigate their stability and gravitational wave emission. We employ five models, both normal and supramassive, and track their evolution with different grid setups and resolutions, as well as with two different evolution codes. We find that all models are dynamically stable and produce a strain that is approximately one-tenth the average value of a merging binary system. We track their secular evolution and find that all our stars evolve towards axisymmetry, maintaining their uniform rotation, rotational kinetic energy, and angular momentum profiles while losing their triaxiality.

I. INTRODUCTION

The discovery of gravitational waves (GWs) from a binary black-hole system [1] was a triumph that initiated a new era in astronomy and astrophysics. Although the prime candidates for the ground-based interferometers are binary systems, GWs from isolated neutron stars (NSs) also can be detected and help reveal the nature of these objects. Out of the ~ 2500 currently known pulsars in our Galaxy, approximately 90% are isolated. Many of these single rotating stars may be promising sources of GWs [2–4].

A single NS can become an emitter of GWs as long as it has a non-spherical time changing quadrupole moment. The lack of symmetry can arise in various scenarios [5–7]. For example, a pulsar can have a “small mountain” that could develop following a starquake in the NS [8, 9], or it can exhibit different kinds of non-spherical oscillations [10]. Another possibility is binary NS mergers, which are themselves prime candidates for the production of GWs. When the two component stars do not have large masses the remnant may not undergo “prompt” collapse, but instead form a hypermassive star and undergo “delayed collapse”, or form a spinning NS that is dynamically and secularly stable [11]. At formation such remnants may be non-axisymmetric and strong GW emitters. A third scenario arises in gravitational stellar collapse, where the bouncing core can be rotating fast enough so that non-axisymmetric instabilities set in and deform the star into an ellipsoid [12]. Fallback accretion onto newly born magnetars also supports the existence of triaxial deformations and the efficient production of GWs [13].

Despite the enormous amount of work done in the field of rotating stars [14, 15] full general relativistic (GR) numerical simulations that investigate the stability and accurately quantify the GW signature of single, uniformly rotating, triaxial stars have not been performed. One of the reasons is the scarcity of accurate initial models needed to study their evolution. Typically these objects are probed in the context of

binary mergers or collapse scenarios, which involve a substantial amount of computational resources and make difficult a systematic parameter study. In these cases one typically ends up with a differentially rotating object while for single, isolated NSs one is often interested in uniformly rotating stars, the GR analogues of Jacobi ellipsoids in Newtonian theory. Such solutions have been obtained for the first time by Nozawa [16] allowing azimuthal dependence in the space-time metric, but restricted it to an axisymmetric form. Using a different method, triaxial quasi-equilibrium models have been computed without such a restriction in the conformal flatness approximation [17] and in the waveless approximation [18] as part of the COCAL code.

The ab initio computation of such non-axisymmetric objects presents a number of challenges. First, these objects are not stationary equilibria, since they emit GWs, and therefore an approximate scheme has to be applied in order to find quasi-stationary solutions. This choice has to be compatible with the fact that the radiated energy within one rotational period is much smaller than the binding energy of the star. Second, such models are known to exist only for stiff equations of state (EoS). If we assume a polytropic law $p = k\rho_0^\Gamma$, where ρ_0 is the rest-mass density and k, Γ are constants, then Γ needs to be larger than 2.24 in the Newtonian limit [19]. For softer EoS mass shedding appears at lower angular velocity than the one needed to reach the triaxial state. GR increases the critical value of the polytropic index by a small amount (to $\Gamma \sim 2.8$) [20]. Third, uniformly rotating, non-axisymmetric solutions exist only for high spin rates, i.e. $\beta := T/|W|$ larger than 0.14 in the Newtonian case [21]. Here T is the rotational kinetic energy and W the gravitational potential energy. In GR this critical value is higher [22–28]. The combination of the above characteristics imply that an evolutionary follow-up will also be nontrivial, since the first challenge described above will imply the presence of junk initial radiation, which must be controlled, while the second and third challenges require higher resolution than for slowly rotating stars. Since the GW timescale to radiate the rotational energy

is $t_{\text{GW}}/M \gtrsim (M/R)^{-4}$ only highly compact objects can be evolved to their endpoint state, while lower compaction stars can be studied only partially. High compaction requires higher resolution, which increases the computational demands even more.

The dynamical stability of the quasi-equilibrium solutions obtained in [17, 18] is not yet known. If these objects are dynamically unstable, do they undergo prompt collapse to black holes, or do they evolve to significantly different, stable, axisymmetric equilibria by rearranging their mass and/or angular momentum profiles? If they are dynamically stable, their secular fate is still unknown. Being non-axisymmetric and rotating they will generate GWs, which will radiate both energy and angular momentum. Will this lead to delayed collapse to a black hole, or will it lead to the formation of a Dedekind-like configuration, or something less exotic?

In [29, 30] the *dynamical* stability of axisymmetric, differentially rotating stars (even including an initial perturbation) has been studied numerically in GR and it was found that they are stable against quasi-radial collapse and bar-mode formation for sufficiently small β . GR enhances the dynamical bar-mode formation since the critical value for $\beta = \beta_{\text{dyn}}$ above which the stars become dynamically unstable was found to be ~ 0.24 , slightly less than the corresponding Newtonian value 0.27 for incompressible Maclaurin spheroids. A precise determination of the threshold for the dynamical instability, the effects of stellar compaction on that, as well as the timescale of the persistence of the bar deformation have been studied in [31–34]. In [35–37] linear stability analysis and simulations have been performed to analyze the occurrence of the dynamical instability against non-axisymmetric bar mode deformation for differentially rotating stars. It was found that when differential rotation is high, the stars are dynamically unstable even when β was of order of 0.01. This dynamical instability does not create spiral arms [38–43] or fragmentation, but drives the star into a quasi-stationary ellipsoid that emits GWs.

The *secular* bar-mode instability induced by GWs with a polytropic ($\Gamma = 2$) EoS in the 2.5 post-Newtonian framework for rapidly rotating stars with $\beta \sim 0.2 - 0.25$ has been investigated in [44]¹. They tracked the evolution of the bar-mode up until the final object was a deformed ellipsoid which was still emitting GWs (therefore was not a Dedekind-like star). At the same time the nonlinear development of the secular bar-mode instability using a stiffer EoS ($\Gamma = 3$) and similarly including post-Newtonian terms for the gravitational radiation reaction was investigated in [46]. Although they were able to reach a “Dedekind-like” state, this was destroyed after ten dynamical times. According to the authors the reason could be either the nonlinear coupling of various oscillatory modes in the star, or an “elliptic flow” instability which manifests itself when the fluid flow is forced along elliptic streamlines.

In a previous work [47] we computed for the first time triaxial *supramassive* NSs (uniformly rotating models with rest-

mass higher than the maximum rest-mass of a non-rotating star, but lower than the maximum rest-mass when allowing for maximal uniform rotation), by using a piecewise polytropic EoS. In this work we perform the first evolutions of such stars and try to investigate their stability and GW content. Following [47] we carefully construct five such models: two *normal* ones (uniformly rotating but not supramassive) with compactness 0.1 and 0.25² adopting a stiff ($\Gamma = 4$) EoS, and three supramassive models with compactness $M/R = 0.23, 0.24, 0.26$ adopting a two-piece polytrope that has a soft core. Although these EoSs are rather extreme, our goal is to prove a matter of principle rather than focus on realistic EoSs. For a single polytrope a stiffer EoS can sustain a larger triaxial deformation, and hence the maximum mass of the triaxial star relative to that of the spherical star is expected to be larger. However, for the two-piece polytropic EoS, the maximum mass of the triaxial star relative to the spherical counterpart increases, even though the overall averaged stiffness of the EoS is softer. If the mass difference between the maximum axisymmetric and triaxial solutions is $\sim 10\%$ or less, then that implies that the EoS of high density matter becomes substantially softer in the core of NSs [47].

We were able to follow the evolution of these objects for more than twenty rotation periods, proving that they are *dynamically stable*. After an initial short period of time where junk radiation in the initial data propagates away, the NS evolves along quasi-equilibrium states that satisfy the first law, $dM = \Omega dJ$. Along this trajectory the orbital angular velocity remains constant inside the NS, whose triaxial shape evolves toward axisymmetry. During this period the GW amplitude decreases significantly, especially in the highly compact models. The question that arises is: are we probing the secular fate of the stars or is this clear monotonic amplitude decrease an artifact of numerical dissipation.

We do not think that the decrease of the GW amplitude is due to numerical viscosity. We performed a resolution study which did not alter the main description above. We discuss the trigger for the declining amplitude below.

If our models are imagined to sample bar-mode perturbations of an axisymmetric configuration with $\beta > \beta_{\text{sec}}$ then according to well-known results [45], our stars should be secularly unstable. We weren’t able to find any growth of a bar-mode. As in [48], where evolutions of models with β larger than β_{sec} with an initial bar-mode perturbation were performed, we find the decay of the initial perturbation.

Here we employ geometric units in which $G = c = M_{\odot} = 1$, unless stated otherwise. Greek indices denote spacetime dimensions (0,1,2,3), while Latin indices denote spatial ones (1,2,3).

II. METHODS AND PHYSICAL PARAMETERS

The numerical methods used here are those implemented in the COCAL and ILLINOIS GRMHD codes, and have been

¹ The critical β for instability in Newtonian Maclaurin spheroids is $\beta_{\text{sec}} \sim 0.14$, but decreases in GR as the compaction increases [45]

² These are the corresponding compactnesses of the spherical solutions.

Γ	$(p/\rho_0)_c$	ρ_c	$(\rho_0)_c$	M_0	M	M/R
4	1.334	0.004658	0.003224	2.882	2.250	0.3552
(4, 2.5)	0.5674	0.006175	0.004536	1.960	1.657	0.2871

TABLE I. Characteristic quantities for the maximum mass spherical solutions of the two EoSs considered in this work. Here Γ denotes the polytropic index, $(p/\rho_0)_c$ the central pressure-to-rest-mass-density ratio, ρ_c the central total energy density, M_0 the rest mass, M the gravitational mass, and M/R the compaction of the star. First line refers to simple polytrope models G4C010, G4C025, while second line to piecewise models pwC023, pwC024, pwC026. To convert to cgs units multiply mass, density and pressure by 1.989×10^{33} g, 6.173×10^{17} g/cm³, and 5.548×10^{38} g/(cm sec²), respectively.

described in great detail in our previous works [49–59], so we only summarize the most important features here.

A. Initial data

Our initial rotating star spacetimes possess a helical Killing vector, k^α , that Lie-drags the fluid variables,

$$\mathcal{L}_k(hu_\alpha) = \mathcal{L}_k\rho_0 = \mathcal{L}_k s = 0. \quad (1)$$

Here u^α is the 4-velocity of the fluid, ρ_0 , h , s are the rest-mass density, enthalpy, and the entropy per unit rest-mass. We have $\rho_0 h = \rho + p$, where ρ is the total energy density and p is the pressure.

For the helical Killing vector we follow the definition of [60] (see also [61]). We decompose k^α as

$$k^\alpha = t^\alpha + \Omega\phi^\alpha, \quad (2)$$

where we choose t^α and ϕ^α to be the time and azimuthal coordinate basis vectors associated with an asymptotically inertial observer, and Ω the angular velocity of the fluid with respect to the same observer. In a chart $\{t, x^i\}$, where x^i are Cartesian coordinates, it is $t^\alpha = \delta_0^\alpha$, and $\phi^\alpha = (0, \phi^i) = (0, -y, x, 0)$. The 4-velocity of the fluid will then be along the helical Killing vector, i.e. there is a scalar u^t such that

$$u^\alpha = u^t k^\alpha = u^t(t^\alpha + \Omega\phi^\alpha) = \alpha u^t(n^\alpha + U^\alpha). \quad (3)$$

In the above, $v^i = \Omega\phi^i$ is the velocity with respect to the inertial frame, while U^α is the spatial velocity with respect to normal observers (those with 4-velocity n^α). In the last equality, α is the lapse function, that normalizes the normal vector to the spacelike hypersurfaces which foliate the spacetime, $n_\alpha = -\alpha\nabla_\alpha t$.

For a perfect gas stress-energy tensor and an isentropic initial configuration the equations of motion yield a first integral,

$$\frac{h}{u^t} = \mathcal{E}, \quad (4)$$

where \mathcal{E} is a constant. The two constants that appear in our equations $\{\Omega, \mathcal{E}\}$ are determined via an iterative scheme. For the gravitational fields we use the Isenberg-Wilson-Mathews

	Initial data models				
	G4C010	G4C025	pwC023	pwC024	pwC026
$\rho_0(\times 10^{-3})$	1.005	1.565	1.902	1.991	2.226
$\rho(\times 10^{-3})$	1.019	1.644	2.065	2.176	2.477
R_x	7.677	7.429	7.774	7.625	7.266
R_z/R_x	0.4727	0.4957	0.4977	0.5015	0.5108
R_y/R_x	0.7500	0.9063	0.9219	0.9375	0.9688
e_z	0.8812	0.8685	0.8673	0.8652	0.8597
ΩM	0.01823	0.08043	0.07850	0.08237	0.09138
P (Period)	193.8	138.3	140.8	137.7	130.4
M	0.5623	1.771	1.760	1.805	1.896
M_0	0.5900	2.012	1.989	2.047	2.169
J/M^2	1.109	0.8516	0.8279	0.8202	0.8003
$(M/R)_s$	0.1000	0.2500	-	-	-
M/R_x	0.07324	0.2383	0.2264	0.2367	0.2610
$T/ W $	0.1543	0.1773	0.1666	0.1661	0.1633
I	10.81	58.77	57.46	58.51	59.70
ε_z	0.2320	0.05581	0.02771	0.0191	0.006200
$\delta M(\times 10^{-4})$	0.8237	0.9893	1.129	1.063	1.007
VE($\times 10^{-4}$)	12.13	5.463	8.047	7.753	7.546
Quadrupole estimates					
$\dot{E}(\times 10^{-8})$	2.846	14.01	2.918	1.548	0.2017
$\dot{J}(\times 10^{-7})$	8.778	30.84	6.540	3.391	0.4186
$rh/M(\times 10^{-3})$	14.63	7.357	3.441	2.389	0.7774
Timescales					
t_d/M	50	10	10	10	10
t_s/M	10^5	10^5	10^6	10^6	10^7

TABLE II. Models G4C010, G4C025 are described by a $\Gamma = 4$ EoS, while models pwC023, pwC024, pwC026 are described by a piecewise-polytropic EoS with polytropic indices $(\Gamma_1, \Gamma_2) = (4, 2.5)$ and are supramassive. Here ρ_0 is the rest-mass density, ρ is the total energy density, R_i are the coordinate radii, $e_z = \sqrt{1 - (R_y/R_x)^2}$ is the eccentricity with respect to the z-axis, Ω is the the angular velocity of the fluid, P is the period, M is the ADM mass, M_0 is the rest-mass, J is the ADM angular momentum, $(M/R)_s$ is the corresponding spherical compaction, $\beta = T/|W|$ is the rotational-to-gravitational-potential-energy ratio, I is the moment of inertia, ε_z is the ellipticity with respect to the z-axis (Eq. A9), \dot{E} is the luminosity, \dot{J} is the angular momentum loss rate, h is the GW maximum amplitude as predicted by the quadrupole approximation applied on the initial data configurations, r is the distance to the source, t_d is the dynamical timescale [see. Eq. (9)], t_s the secular timescale [see Eq. (12)]. Finally, δM and VE are diagnostics to measure the accuracy of the initial data defined in Eq. (5) and in Eq. (A14) of [18], respectively. To convert to geometric $G = c = 1$ or cgs units, use the fact that $1 = 1.477$ km = $4.927 \mu\text{s} = 1.989 \times 10^{33}$ g.

(IWM) approximation [68, 69] which assumes a flat conformal metric and maximal slicing. The resulting five elliptic equations are solved together with Eq. (4) and coupled to a piecewise EoS as described in [17, 18].

A number of diagnostics are used to describe the initial solutions and explicit formulae are given in the appendix of [18]

and will not be repeated here. Since the IWM formulation is used, we have that $\gamma_{ij} = \psi^4 f_{ij}$, where γ_{ij} is the spatial metric on the hypersurface, ψ is the conformal factor and f_{ij} the flat metric in spherical coordinates. The angular momentum $J = J_{\text{ADM}}$ [where J_{ADM} is the Arnowitt-Deser-Misner (ADM) angular momentum] is computed via a surface integral at infinity or a volume integral over the spacelike hypersurface. The kinetic rotational energy is defined as $T := \frac{1}{2} J \Omega$ (although we are not in axisymmetry we still use this formula because it is gauge-invariant), and the gravitational potential energy is defined as $W := M_{\text{ADM}} - M_{\text{P}} - T$. Here $M_{\text{ADM}} = M$ is the (ADM) mass and M_{P} is the rest-mass plus internal energy of the star (see e.g. [70]). These expressions are used then to compute the rotation parameter β . Also the moment of inertia is defined as $I := J/\Omega$. As a measure of accuracy of the initial data we provide two diagnostics: The first one is the difference between the Komar and ADM mass,

$$\delta M = \frac{|M_{\text{K}} - M_{\text{ADM}}|}{M_{\text{K}}}. \quad (5)$$

For stationary and asymptotically flat spacetimes $M_{\text{K}} = M_{\text{ADM}}$ ³ [72]. The second diagnostic is the relativistic virial equation (VE) [73].

The initial-data GW diagnostics involve the second mass moments

$$I^{ij} := \int_{\Sigma_t} \rho_0 u^\alpha x^i x^j dS_\alpha \quad (6)$$

with $dS_\alpha = \nabla_\alpha t \sqrt{-g} d^3x$. In Appendix A we have derived some useful quantities such as the quadrupole approximation for the luminosity and the GW amplitude, that can be computed on a spacelike hypersurface in the presence of a helical Killing vector. However, full GW output, including the “junk” radiation inherent in the initial data, is computed in full GR as part of the integration of the field equations via the Baumgarte-Shapiro-Shibata-Nakamura (BSSN) formalism [62, 63].

As in [47] we employ the same “benchmark” EoSs. The first one is a simple $\Gamma = 4$ polytrope, while the second is a piecewise-polytropic EoS with two pieces and a soft core, where $\{\Gamma_1, \Gamma_2\} = \{2.5, 4\}$. Characteristics of the maximum mass solutions for spherical stars using these two EoSs are reported in Table I. The adiabatic constant k , is chosen so that the value of the rest-mass becomes $M_0 = 1.5$ (in units of solar mass) at the compaction $M/R = 0.2$. By choosing different values of k one can attain larger maximum masses. A well-known fact that relates the maximum masses of those models, is that a stiffer EoS can sustain a larger maximum mass (see below). The same result holds for the maximum

³ Although for non-axisymmetric systems the helical Killing vector (stationarity in the rotating frame) is incompatible with asymptotic flatness [71], one can define an approximate asymptotic region in which the GW energy is small compared with the total energy of the system. The same argument holds for the existence of the Komar mass that is associated with a timelike Killing field t^α .

$r_a = 0$: Radial coordinate where the radial grids start.
$r_b = 10^6$: Radial coordinate where the radial grids end.
$r_c = 1.25$: Radial coordinate between r_a and r_b where the radial grid spacing changes.
$N_r = 384$: Number of intervals Δr_i in $r \in [r_a, r_b]$.
$N_r^f = 128$: Number of intervals Δr_i in $r \in [r_a, 1]$.
$N_r^m = 160$: Number of intervals Δr_i in $r \in [r_a, r_c]$.
$N_\theta = 96$: Number of intervals $\Delta \theta_j$ in $\theta \in [0, \pi]$.
$N_\phi = 96$: Number of intervals $\Delta \phi_k$ in $\phi \in [0, 2\pi]$.
$L = 12$: Order of included multipoles.

TABLE III. Summary of grid parameters used by COCAL to produce the five models. $N_r^f = 128$ is the number of points across the largest star radius which extends from $r = 0$ to $r = 1$ in COCAL coordinates, while $N_r = 384$ is the total number of radial points. The radial grid is equidistant from $r = 0$ to $r = r_c$, and non-equidistant thereafter. The angular grids are equidistant with $\Delta \theta_j = \pi/N_\theta$, and $\Delta \phi_k = 2\pi/N_\phi$ in the θ and ϕ directions respectively. For more details on the grids used by COCAL see [18].

masses of the axisymmetric solutions. The values of Γ used are simply to prove a point of principle, rather than address physical EoS parameters: stiffness is necessary in order for these triaxial solutions to exist. A higher value of Γ satisfies the necessary conditions for uniformly rotating triaxial solutions to exist, and this is the main reason behind such a choice. As discussed in [47] the softening of the core enables us to compute for the first time supramassive, triaxially deformed, uniform rotating stars, without increasing further the maximum polytropic exponent Γ . This was made possible from the following counter-intuitive fact which does not depend on the values of the specific polytropic indices: Assume a simple (any $\Gamma > 2.24$) polytrope which in most cases does not support supramassive triaxial solutions. Then consider a second two piece polytropic EoS $\{\Gamma_1, \Gamma_2\}$, with $\Gamma_2 = \Gamma$ and a soft core with $\Gamma_1 < \Gamma$. This second EoS is effectively softer than the first. Thus one expects that the piecewise EoS does not exhibit triaxial solutions with mass larger than the maximum-mass spherical solution. This was proven not to be the case [47], and if the relative difference between the maximum triaxial and axisymmetric masses is less than 10%⁴ it provides strong evidence of softening in the core of the compact object.

In order to investigate the stability and GW signature of such solutions we consider five models, G4C010, G4C025, pwC023, pwC024, and pwC026 whose characteristics are reported in Table II⁵. The last three columns are supramassive solutions while the others are normal ones. The triaxiality⁶ is

⁴ The maximum mass of triaxial solutions is always smaller than the maximum mass of axisymmetric ones.

⁵ As we mentioned in the introduction all quantities reported are in $G = c = M_\odot = 1$ units. This means that if one wants to convert mass to geometric $G = c = 1$ units one has to multiply by 1.477 km. For the angular velocity Ω , one divides by 1.477 km. Similarly to get Ω in cgs units again one divides by 4.927 μs .

⁶ Triaxiality is not used in any quantitative way in this paper. It can be de-

larger for the first column model and diminishes as we move to more compact stars. This means that the amplitude of the GW will be larger for the first model and smaller for the last one.

The models have been computed with the COCAL code, a second-order finite-difference code whose methods are explained in [50–54]. For single compact objects it employs a single spherical patch (r, θ, ϕ) with $r \in [r_a, r_b]$, $\theta \in [0, \pi]$, and $\phi \in [0, 2\pi]$, where $r_a = 0$, $r_b = O(10^6 M)$, and M the total mass of the system (no compactification used). The grid structure in the angular dimensions is equidistant but not in the radial direction. The definitions of the grid parameters can be seen in Table III, along with the specific values used to obtain the quasi-equilibrium solutions of this work.

B. Evolution

For the evolution we use the ILLINOIS GRMHD code⁷, which solves the Einstein field equations in the BSSN formalism [62, 63, 70]. The code is built on the CACTUS [76] infrastructure and uses CARPET⁸ for mesh refinement, which allows us to focus numerical resolution on the strong-gravity regions, while also placing outer boundaries at large distances well into the wave zone for accurate GW extraction and stable boundary conditions. The evolved geometric variables are the conformal metric $\tilde{\gamma}_{ij}$, the conformal factor ϕ , ($\gamma_{ij} = e^{4\phi}\tilde{\gamma}_{ij}$), the conformally-rescaled, trace-free part of the extrinsic curvature, \tilde{A}_{ij} , the trace of the extrinsic curvature, K , and three auxiliary variables $\tilde{\Gamma}^i = -\partial_j \tilde{\gamma}^{ij}$, a total of 17 functions. For the kinematic variables we adopt the puncture gauge conditions [77–79], which are part of the family of gauge conditions using an advective “1 + log” slicing for the lapse, and a “Gamma-driver” for the shift [80].

The equations of hydrodynamics are solved in conservation-law form adopting high-resolution shock-capturing methods [56, 57]. The primitive, hydrodynamic matter variables are the rest mass density, ρ_0 , the pressure p and the coordinate three velocity $v^i = u^i/u^0$. The enthalpy is written as $h = 1 + \epsilon + p/\rho_0$, and therefore the stress energy tensor is $T_{\alpha\beta} = \rho_0 h u_\alpha u_\beta + p g_{\alpha\beta}$. Here, ϵ is the specific internal energy⁹.

To close the system an EoS needs to be provided and for that we follow [58, 59] where the pressure is decomposed as a sum of a cold and a thermal part,

$$p = p_{\text{cold}} + p_{\text{th}} = p_{\text{cold}} + (\Gamma_{\text{th}} - 1)\rho_0(\epsilon - \epsilon_{\text{cold}}) \quad (7)$$

finned in various ways, like R_y/R_x , e_z , or ε_z (see Table II) and signifies the departure from axisymmetry. In GW detection studies, triaxiality is measured by the ellipticity ε_z . Notice that the ellipticities of the models we consider here are larger than typical limits set by LIGO [74]. However, as isolated pulsars are dim and hard to find, there could exist a population of undetected pulsars that LIGO has not probed, yet.

⁷ We do not use ILLINOIS GRMHD, which is the version of the code embedded in the Einstein Toolkit [75].

⁸ <http://www.carpetcode.org>

⁹ This should not be confused with the ellipticity ε_z .

where

$$\epsilon_{\text{cold}} = - \int p_{\text{cold}} d(1/\rho_0) = \frac{k}{\Gamma-1} \rho_0^{\Gamma-1} + \text{const.} \quad (8)$$

Here k, Γ are the polytropic constant and exponent of the cold part (same as the initial data EoS) and $\Gamma_{\text{th}} = 5/3$. The constant that appears in the formula above is zero for a single EoS, but takes different values in a piecewise polytrope where one has to account for the continuity of pressure at the join between the different pieces.

The grid structure used in these evolutions is summarized in Table IV. Typically we use six refinement levels with the innermost level half-side length being approximately ~ 1.25 times larger than the radius of the star in the initial data (R_x). We use $240 \times 240 \times 120$ points for the innermost refinement level, which means that we have approximately 190 points across the NS largest diameter. (For the initial data construction we used 256 points across the largest NS diameter.) For the innermost refinement level this implies a $\Delta x \sim 0.07916 = 117$ m. This number of points was necessary in order to have accurate evolutions of such stiff EoS ($\Gamma = 4$) which present a challenge for any evolution code.

For the last model pwC026 we have done two extra simulations, as the compaction in this case was very high and the triaxiality very low. In this model the GW signal was very weak ($rh/M \sim 10^{-4}$) and therefore we wanted to corroborate our findings by using different resolution and box size for the outer boundary conditions. On the last two lines of Table IV the lower resolution simulation has the same outer boundary distance (288) but 80 points across the star radius, while we have also a simulation with seven refinement levels and the outer boundary at much larger distance (1152.0) than all other cases. In all our models we impose equatorial symmetry.

III. RESULTS

NS mergers remnants can be non-axisymmetric configurations which are initially differentially rotating. However, it is expected that magnetically induced turbulence drives the star toward uniform rotation. This motivates a study of the stability of uniformly rotating, triaxial configurations and an estimate of their GW emission. In particular, it motivates the following questions that we want to address in this work: Can a *uniformly* rotating triaxial star be dynamically stable? If that is possible, what is the secular fate of such a configuration?

A. Dynamic stability

The dynamical timescale for our stars is

$$\frac{t_d}{M} \sim \frac{1}{\Omega M} \sim \left(\frac{M}{R}\right)^{-3/2}, \quad (9)$$

and values range from ~ 10 for the most compact cases to ~ 50 for G4C010, the least compact model (see Table II). We find that all of the models considered are dynamically stable.

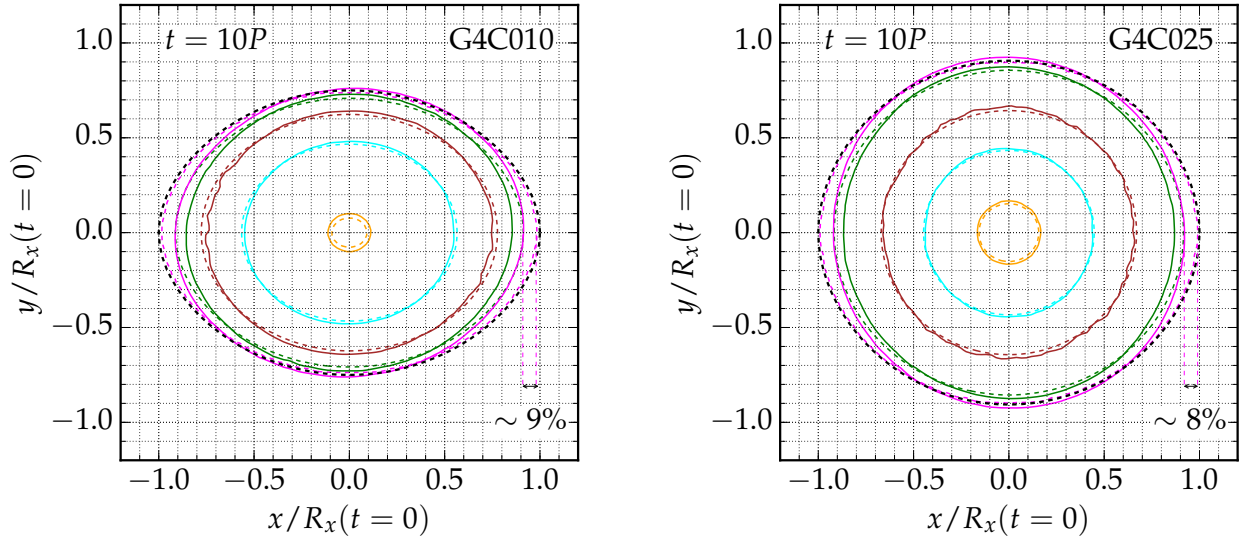


FIG. 1. Contour plots on the xy -plane of the rest-mass density ρ_0 for the normal models G4C010 and G4C025. Distances are normalized by the initial data radius along the x -axis $R_x(t=0)$. The black dashed line signifies the initial data surface, while dashed color lines correspond to $t=0$ level lines of densities $\{0.2, 0.4, 0.6, 0.8, 1.0\} \times 10^{-3}$ for the G4C010 model. The same color but solid lines correspond to the same density levels after ten rotation periods. The contour plots of the G4C025 model correspond to $\{0.2, 0.5, 1.0, 1.3, 1.53\} \times 10^{-3}$. To convert densities to cgs units multiply by $6.173 \times 10^{17} \text{ g/cm}^3$.

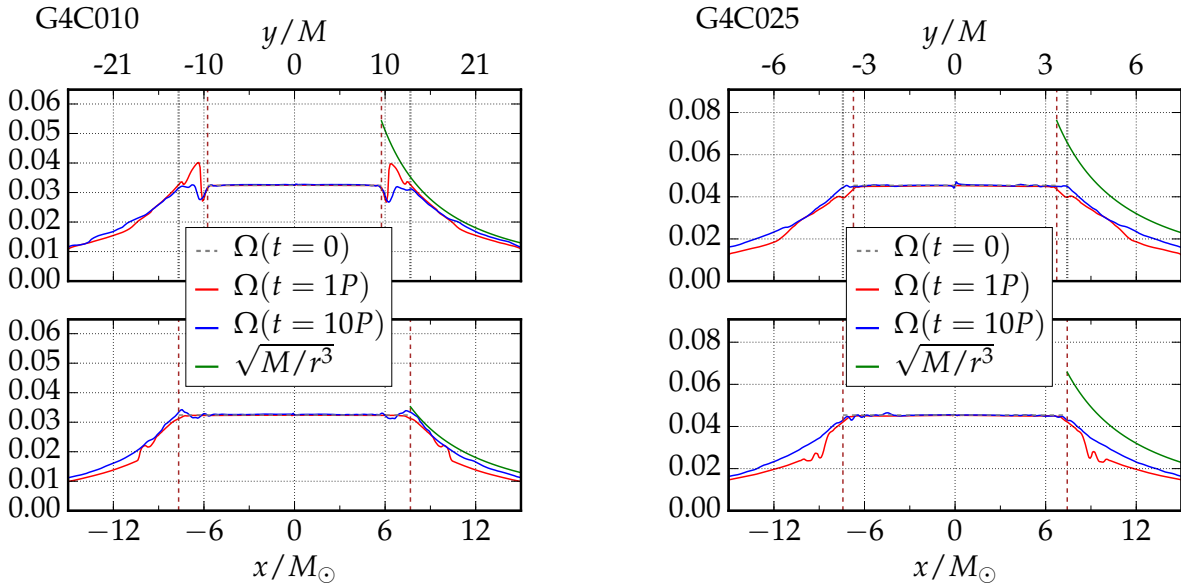


FIG. 2. Angular velocity profile across the x -axis (bottom) and the y -axis (top) for the normal models G4C010 and G4C025. The horizontal gray, dashed line corresponds to the initial data Ω and extends only in the interior of the star (this curve is difficult to see since it coincides with the red and blue curves inside the star). Red and blue solid lines correspond to the angular velocity after one and ten rotation periods, while the green line is the Keplerian limit $(M/r^3)^{1/2}$. Vertical brown dashed lines corresponds to the initial data radii along the x and y axes. Vertical dotted gray lines on the top figures denote the initial radii along the x -axis. To convert Ω in cgs units divide by $4.927 \mu\text{s}$.

Model	x_{\min}	x_{\max}	y_{\min}	y_{\max}	z_{\min}	z_{\max}	Grid hierarchy	dx	N
G4C010	-304	304	-304	304	0	304	{9.5, 19.0, 38.0, 76.0, 152.0, 304.0}	$2.5\bar{3}$	96
G4C025	-304	304	-304	304	0	304	{9.5, 19.0, 38.0, 76.0, 152.0, 304.0}	$2.5\bar{3}$	93
pwC023	-304	304	-304	304	0	304	{9.5, 19.0, 38.0, 76.0, 152.0, 304.0}	$2.5\bar{3}$	98
pwC024	-304	304	-304	304	0	304	{9.5, 19.0, 38.0, 76.0, 152.0, 304.0}	$2.5\bar{3}$	96
pwC026	-288	288	-288	288	0	288	{9.0, 18.0, 36.0, 72.0, 144.0, 288.0}	2.4	96
pwC026-I	-288	288	-288	288	0	288	{9.0, 18.0, 36.0, 72.0, 144.0, 288.0}	2.88	80
pwC026-II	-1152	1152	-1152	1152	0	1152	{9.0, 18.0, 36.0, 72.0, 144.0, 288.0, 576.0}	9.6	96

TABLE IV. Grid parameters used for the evolution of each model. Parameter N corresponds to the number of points used to cover the largest radius of the star. Parameter dx is the step interval in the coarser level. We impose reflection symmetry across the equatorial plane. To convert to physical units multiply by $1 = 1.477$ km.

Figure 1 shows typical contour plots at $t = 0$ (dashed colored lines) as well as the same contour plots after ten rotation periods (solid colored lines). The black dashed line signifies the initial data surface of the star in the xy -plane as calculated by COCAL. Of particular importance are the lowest density contours at $\rho_0 = 0.0002 = 9.16788 \times 10^{-15} \text{ cm}^{-2}$ (magenta colored). The choice of this particular value can be considered as one of the largest densities that follow closely the initial data profile (black dashed line). By following the evolution of this contour one can have an accurate picture of the surface of the star. After the junk radiation has propagated away the stars still retain their triaxiality. But by $t = 10 P$, all contours tend to circularize (the one of the highest density is initially circular). All these contours contract in the x -direction and expand in the y -direction. The amount of contraction/expansion diminishes as one moves towards the center of the star. Thus the star becomes more axisymmetric. After ten periods the x -axis has lost 9–8% of its length. For the supramassive models this picture still holds, although since the ellipticities there are much smaller the amount of contraction/expansion is somewhat diminished. For the most supramassive model, pwC026, after ten rotation periods the decrease is $\sim 4\%$ and the object is essentially axisymmetric. While density contours are not gauge-invariant, they yield a qualitative picture that agrees with the GW signature that we discuss in the next section.

The constant angular velocity profile is well preserved (Fig. 2). The angular velocity across the x -axis (bottom panels) and the y -axis (top panels) is plotted for the G4C010 and G4C025 models. Red curves correspond to Ω after one rotation period while blue curves after ten rotation periods. Vertical brown dashed curves denote the initial data star radii, and the green curve is the Keplerian limit $\Omega_K = (M/r^3)^{1/2}$. The less compact the star the closest to the Kepler limit is the “atmospheric tail” outside the surface of the star. Although the y -axis starts shorter than the x -axis after ten rotation periods it has “closed the gap” and the two axes have essentially identical angular velocity profiles (this gap is the space between vertical brown dashed and gray dotted lines). This effect is more evident in the G4C010 model but can be clearly seen in the other most compact cases like G4C025.

B. Secular fate

Although dynamic stability was straightforward to establish, that has not been the case with secular stability. After evolving for more than twenty rotational periods one can see in Fig. 3 the major characteristics of GW emission. The ordinate in the plots is the retarded time $t_{\text{ret}} = t - r_*$, where $r_* = R_a + 2M \ln(R_a/(2M) - 1)$ is the tortoise coordinate corresponding to areal radius R_a from the source. The frequency of the dominant ($l = m = 2$) GW mode is twice the rotational frequency, and has amplitude approximately one-tenth of the average value of a merging binary system. The quadrupole-approximation prediction for the GW strain based on the initial configurations is given by Eq. A6, and is shown in the plots as a dashed horizontal green line. This approximate value for the strain is about 50–60% of the maximum amplitude found in the evolution (see also Fig. 4). The GW amplitude in the more compact models (G4C025) experiences a more rapid decrease (almost ten times more) than in the G4C010 case, which has the smallest compaction ($M/R = 0.1$). Similar behavior is exhibited in the luminosity and radiated angular momentum plots. In all cases, after an initial period that lasts a little over $500 M_\odot$ ($M_\odot = 4.927 \mu\text{s}$) \dot{E} and \dot{J} intersect the predictions from the quadrupole approximation based on the initial-data (in the plots these are denoted by the horizontal blue and red dashed lines, Eqs. A2). However, \dot{E} and \dot{J} undergo exponential decay in close agreement with the corresponding exponential decay in the GW amplitude, i.e.,

$$\dot{E} \propto \dot{J} \propto (rh)^2. \quad (10)$$

In Fig. 3 we denote the exponential fits for all relevant functions. The evolutionary path of these rotating objects occurs along quasi-equilibrium states as seen in the left panel of Fig. 5, which shows $dE = \Omega dJ$. After an initial period of $\sim 500 M_\odot$, this law is satisfied in all cases, apart from a small perturbation at $1050 M_\odot$ for the most supramassive case pwC026. As we see from Table IV, the grid structure of pwC026 is very close to that of models G4C010, G4C025, pwC023, pwC024. However, pwC026 is only slightly non-axisymmetric, and, as a result, its GW signal is very weak – approximately one order of magnitude smaller than the rest. Therefore, if the outer boundary is not sufficiently far away re-

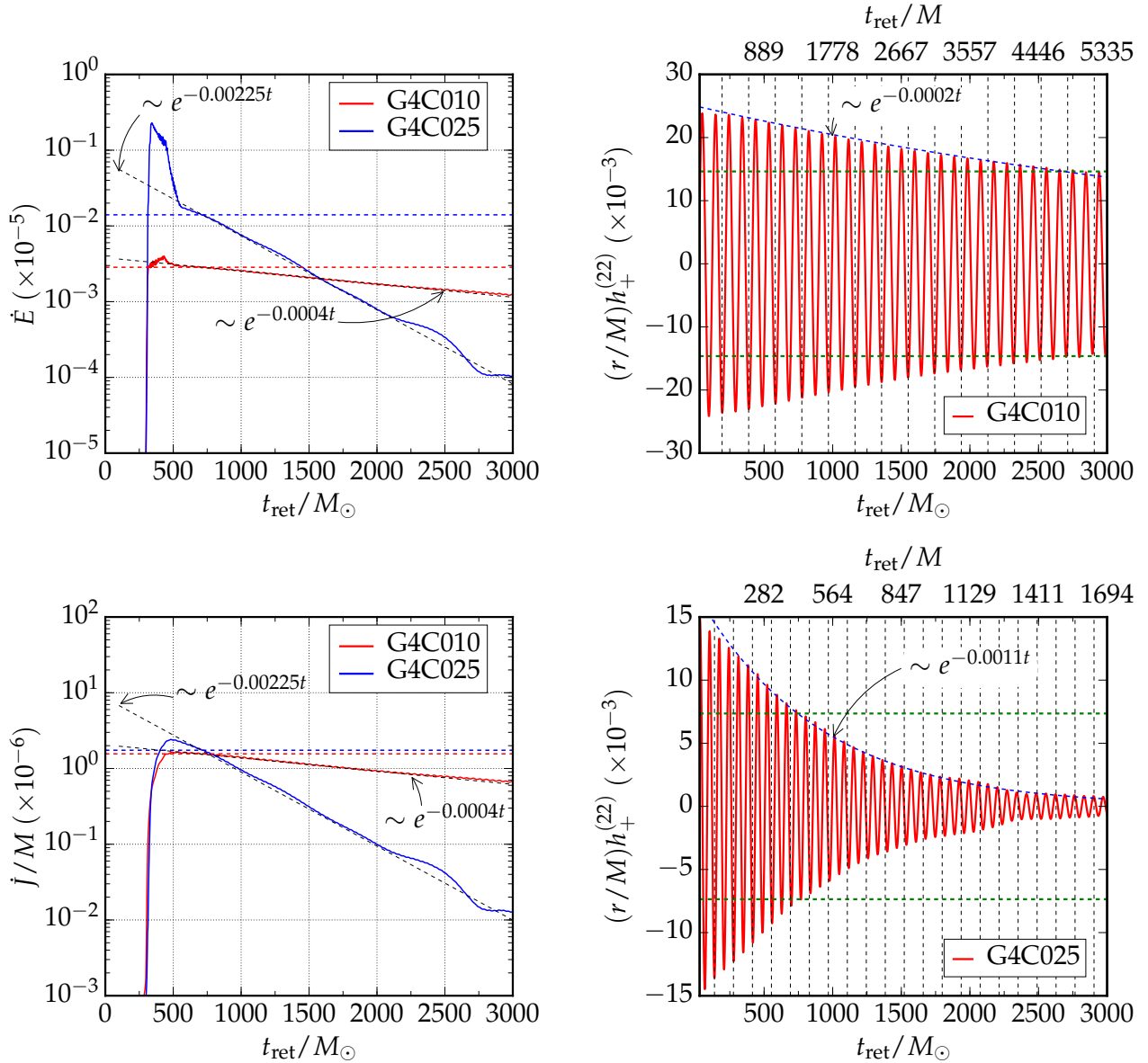


FIG. 3. All plots correspond to the normal models G4C010 and G4C025, and horizontal dashed lines are the initial data quadrupole estimates. Top left is GW power emitted; top right is the dominant $l = m = 2$ mode of the GW strain for the least compact model G4C010, with vertical dashed lines corresponding to rotational periods; bottom left is the emitted angular momentum, and bottom right the strain for the G4C025 model. Also denoted are exponential fitting curves. The GW timescales for the G4C010 and G4C025 models are $1/0.0002 = 8895 M$ and $1/0.0011 = 513 M$ respectively. To convert \dot{E} and j/M to cgs units multiply by $1 = 3.629 \times 10^{59}$ ergs/sec and 8.988×10^{20} ergs/g respectively.

flections from there can alter this weak signal and produce the perturbation seen using the grid pwC026. When we push the outer boundary to larger values like in pwC026-II, this artifact is greatly diminished (blue curve on bottom of Fig. 5). As a final check for the model pwC026 which is the most compact, supramassive and almost axisymmetric we performed a third run using the coarser resolution pwC026-I. Through this lower-resolution run we were able to confirm that the GW characteristics and quantities we quote here are invariant with resolution.

The kinetic (rotational)-to-gravitational-potential-energy ratio β remains essentially constant and is equal to the initial value (see right panel of Fig. 5) during the whole evolution. For the less compact case G4C010, β slightly decays which is consistent with the quasi-equilibrium studies of [18].

The thermal energy generated by shocks was also measured in these simulations by inspecting the entropy parameter $K := p/p_{\text{cold}}$, where $p_{\text{cold}} = k\rho_0^\Gamma$. With $\epsilon_{\text{th}} = \epsilon - \epsilon_{\text{cold}} = (K - 1)(\Gamma - 1)\epsilon_{\text{cold}}/(\Gamma_{\text{th}} - 1)$, then $K > 1$ implies shock heated gas [81]. Since we don't have any mergers in our problem we

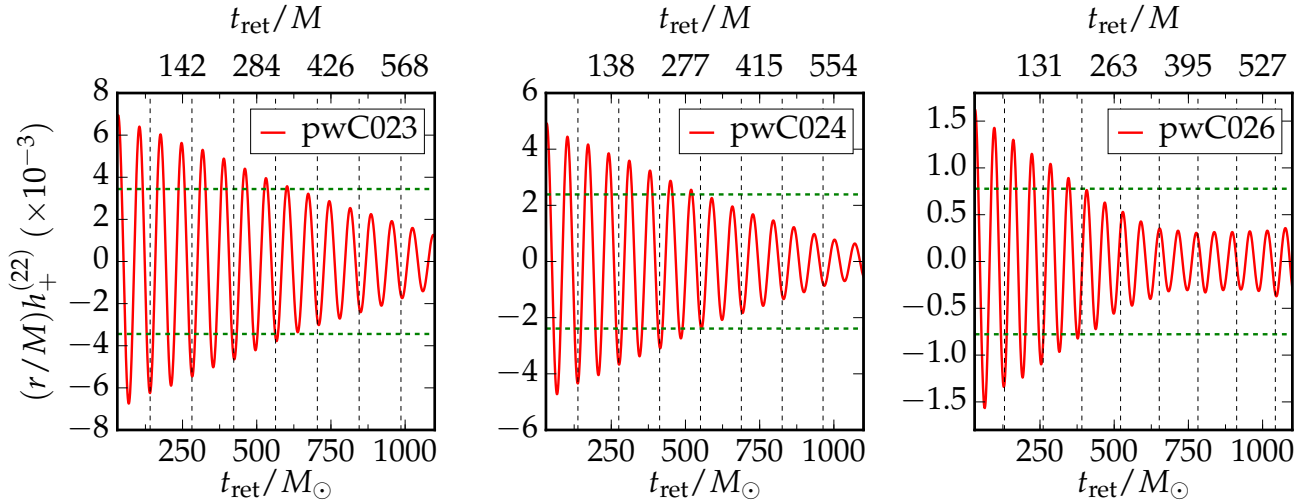


FIG. 4. GW strain for the supramassive models and the $l = m = 2$ mode. Vertical dashed lines correspond to rotational periods, while the horizontal dashed lines denote the quadrupole approximation values.

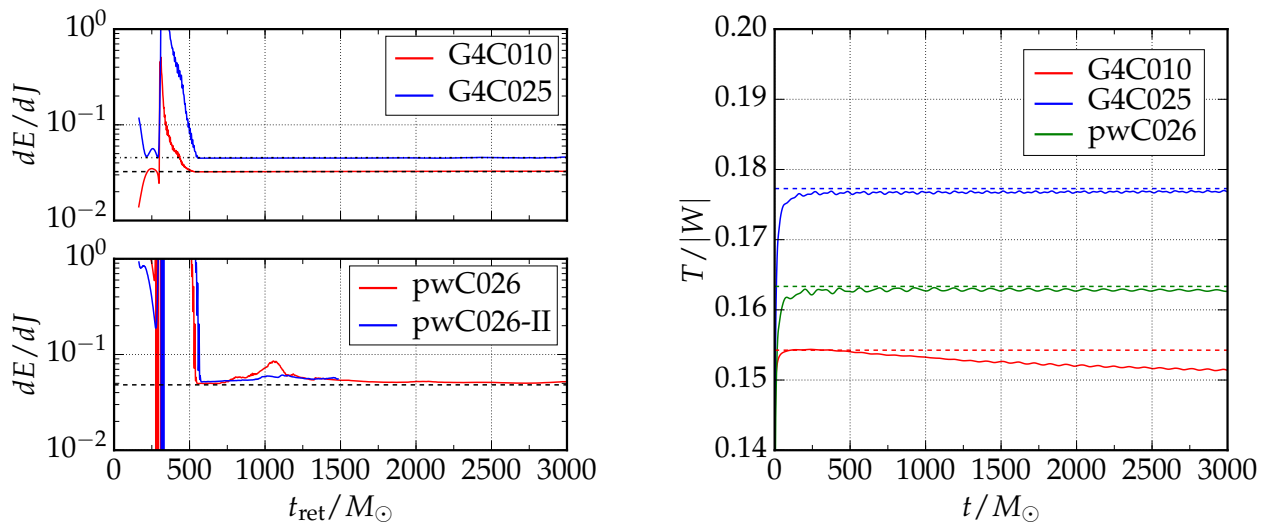


FIG. 5. Left plot: The first law for the triaxially deformed, uniformly rotating NSs. The top panel corresponds to the normal models G4C010 and G4C025, while the bottom one corresponds to the most supramassive case for two different grid setups pwC026 and pwC026-II from Table IV. Dashed lines denote the corresponding initial data angular velocities. To convert dE/dJ is cgs units divide by $4.927 \mu\text{s}$. Right plot: rotational-to-gravitational-potential-energy ratio for the same models. Dashed lines denote the initial data values.

didn't expect any shocks, and this was the case for the bulk of the stars ($K \sim 1.0$).

Although we clearly see that triaxially deformed stars evolve in a quasi-equilibrium manner towards axisymmetric objects, the key question is whether this evolution is due mainly to GW emission or to a hydrodynamical reconfiguration? Using the exponential fitting functions in Fig. 3 we read off the GW decay timescales. These are $5000M_\odot \sim 10^4 M$ for the G4C010 and $900M_\odot \sim 500 M$ for the G4C025 mod-

els. The GW driven bar-mode instability occurs for stars rotating with $\beta > \beta_{\text{sec}}$ and $\beta_{\text{sec}} \approx 0.14$ in the Newtonian incompressible limit. This value decreases in GR as the compaction increases [45]. The two models discussed here have $\beta = 0.15, 0.18$ (see Table II), and are thus greater the Newtonian critical value β_{sec} . The GW timescale is [82]

$$\frac{\tau_{\text{bar}}^{\text{GW}}}{M} \sim 2 \times 10^{-3} \left(\frac{M}{R} \right)^5 (M\Omega)^{-6} (\beta - \beta_{\text{sec}})^{-5}, \quad (11)$$

where β_{sec} may be approximated by $\beta_{\text{sec}} = 0.115 - 0.048M/M_{\text{max}}^{\text{sph}}$ [83]. Here $M_{\text{max}}^{\text{sph}}$ is the maximum spherical mass for the given EoS. For our cases values are taken from Table I, which imply that $\tau_{\text{bar}}^{\text{GW}} \sim 10^8 M$ for the G4C010 and $\tau_{\text{bar}}^{\text{GW}} \sim 10^5 M$ for the G4C025 models, respectively. Supramassive models pwC023, pwC024, pwC026 have timescales $\tau_{\text{bar}}^{\text{GW}} \sim 10^5 M$ too. We also note that the GW timescales as calculated from the crude quadrupole estimate,

$$t_s \sim \frac{T}{|E|}, \quad (12)$$

and reported in Table II, are in most cases (except for G4C010) longer than the timescales obtained from Eq. 11. Moreover, our configurations do not evolve toward Dedekind-like ellipsoids as in the case of the bar-mode unstable Newtonian configurations [12, 84]. It is possible that the nonlinear growth of the instability is halted by mode-mode coupling, as our triaxial configuration contains modes beyond $m = 2$.

Another possibility for a GW driven secular instability is the non-axisymmetric r-mode. For the $l = m = 2$ mode the timescale is [85]

$$\frac{\tau_r^{\text{GW}}}{M} \sim 10 \left(\frac{M}{R} \right)^4 (M\Omega)^{-6}, \quad (13)$$

which implies $\tau_r^{\text{GW}} \sim 10^7 M$ for the G4C010 and $\tau_{\text{bar}}^{\text{GW}} \sim 10^5 M$ for the G4C025 respectively. These timescales again are much longer than the timescales found numerically. Also, in this case the wave frequency $f_{\text{GW}} = 4/3 f_{\text{rot}}$ therefore this possibility is also ruled out by our data, for which $f_{\text{GW}} = 2f_{\text{rot}}$.

Numerical viscosity, although nonzero, can in principle be responsible. The presence of viscosity can damp a GW radiation reaction-induced bar-mode instability [86], although it needs to be properly tuned. However, we evolved with two different resolutions and found no change in the behavior which might have been expected if numerical viscosity were significant. Also we repeated the calculation with the WHISKY code [87–90] and got very similar results. It may be that even a small numerical viscosity over time is sufficient to damp the mode, given the long timescale ($\gg t_{\text{dyn}}$) for GW emission. If we modeled numerical viscosity by a turbulent viscosity $\nu \sim \alpha R c_s \sim \alpha (R/M)^{1/2}$, where c_s is the sound speed, then a damping time of $10^4 M$ associated with this would only require $\alpha \sim 10^{-3}$ to be effective. Such a small value might go unnoticed by a modest resolution study. On the other hand, if viscosity were to dominate GW dissipation, one still expects that the bar mode will be triggered above $\beta = \beta_{\text{sec}}$, since viscosity alone can drive the instability, and the triaxiality would grow [91], but this is not observed. Hence we conclude that although our triaxial stars evolve towards axisymmetry, it is not the bar or r-mode secular effects that are mainly responsible for this fate but rather a hydrodynamical reconfiguration of the initial data.

IV. DISCUSSION

In this work we investigated the stability properties and gravitational wave signatures of uniformly rotating, triaxial NSs in GR. Using the COCAL code we have constructed normal as well as supramassive solutions in quasi-equilibrium and we evolved them for the first time with the ILLINOIS GRMHD code.

All five solutions that we considered are dynamically stable and evolve secularly towards an axisymmetric configuration. Although we monitored the evolution for more than twenty rotation periods we were unable to probe the final (secular) fate of these stars, which is orders of magnitude longer. We corroborated our findings by using different resolutions, placement of outer boundary conditions, atmospheric treatments, and simulations with a different (WHISKY) code.

According to [45] a perturbed axisymmetric star with $\beta > \beta_{\text{sec}}$ will be secularly unstable and develop a bar mode. In our case the initial models already contain a bar perturbation and are rotating beyond the secular bar-mode instability limit, but we found no further growth of a bar mode in the time frame of our simulations, which was shorter than the predicted, theoretical secular timescale. On the contrary we observed the decay of the star's triaxiality, which is in accordance with previous investigations [48].

On the other hand in [18] we constructed sequences of axisymmetric and triaxial stars using both the conformal flatness and the waveless approximation for a simple $\Gamma = 4$ polytrope with compactness $M/R = 0.1, 0.2, 0.3$ (see Fig. 6 in [18]). As we have seen, triaxial sequences for the larger compactness have essentially constant $T/|W|$ all the way from the bifurcation point to the mass shedding limit. The sequence of smaller compactness ($M/R = 0.1$) exhibits a small increase in $T/|W|$ as one moves toward the mass shedding limit. This is consistent with right panel of Fig. 5. Our initial ($t = 0$) triaxial models are highly rotating and are close to the mass shedding limit. The most compact ones (G4C025, pwC026) evolve toward the bifurcation point with a constant $T/|W|$, while the less compact one (G4C010) loses a small amount of rotational energy. Therefore the quasi-equilibrium picture is in agreement with the actual dynamical evolution of such systems in full general relativity.

ACKNOWLEDGMENTS

We thank Cecilia Chirenti, Nikolaos Stergioulas and Enping Zhou, for useful discussions. This work was supported by NSF Grants PHY-1300903, PHY-1602536, PHY-1607449, NASA Grants NNX13AH44G, NNX16AR67G (Fermi), and JSPS Grants-in-Aid for Scientific Research (C) No. 26400274, and 15K05085. VP gratefully acknowledges support from the Simons foundation. This work made use of the Extreme Science and Engineering Discovery Environment (XSEDE), which is supported by National Science Foundation grant number TG-MCA99S008. This research is part of the Blue Waters sustained-petascale computing project, which is supported by the National Science Foundation (awards

OCI-0725070 and ACI-1238993) and the State of Illinois. Blue Waters is a joint effort of the University of Illinois at Urbana-Champaign and its National Center for Supercomputing Applications. Some numerical computations were carried out on the XC30 system at the Center for Computational Astrophysics (CfCA) of the National Astronomical Observatory of Japan.

Appendix A: Quadrupole formulae in helical symmetry

For an estimate of the GWs one can compute the time derivatives of the quadrupole mass moments. Typically the quadrupole formula reads

$$h_{ij}(t, x^a) = \frac{2}{r} \left[\frac{d^2 \mathcal{I}_{ij}^{TT}}{dt^2} \right]_{\text{ret}} \quad (\text{A1})$$

where $\mathcal{I}_{ij} := I_{ij} - \frac{1}{3} f_{ij} I_{kk}$, and \mathcal{I}_{ij}^{TT} is the transverse trace-less reduced quadrupole moment [92]. The second time derivatives are computed at a retarded time. The corresponding gravitational wave luminosity and the angular momentum carried away per unit time are

$$\frac{dE}{dt} = \frac{1}{5} \langle \ddot{\mathcal{I}}_{ij} \ddot{\mathcal{I}}_{ij} \rangle, \quad \frac{dJ^i}{dt} = \frac{2}{5} \epsilon^{ijk} \langle \dot{\mathcal{I}}_{ja} \dot{\mathcal{I}}_{ka} \rangle, \quad (\text{A2})$$

where $\langle \cdot \rangle$ denote an average over several wavelengths. In full dynamical spacetimes there is no unique definition of the quadrupole moment but typically one uses Eq. (6) as a generalized integral over the hypersurface Σ , [93] which can be thought as an Euclidean integral over a weighted density $\rho_* = \rho_0 u^t \sqrt{-g}$. Its time derivative

$$\frac{d}{dt} I_{ij} = \int_{\Sigma} \rho_0 u^\alpha (x_i v_j + x_j v_i) dS_\alpha, \quad (\text{A3})$$

can be obtained by using the conservation of rest mass $\partial_t \rho_* + \partial_i (\rho_* v^i) = 0$, and integration by parts [94].

Another way to obtain the same result is to employ the transport theorem that says that for any density ρ_* that satisfies the above continuity equation and any function $Q(t, x^i)$, we have

$$\frac{d}{dt} \int_{V_t} \rho_* Q dV = \int_{V_t} \rho_* \frac{DQ}{Dt} dV, \quad (\text{A4})$$

where $\frac{DQ}{Dt} = \partial_t Q + v^i \partial_i Q$ is the Lagrangian derivative of Q . For a fluid velocity $v^i = \Omega \phi^i$, we have $DQ/Dt = \mathcal{L}_{\mathbf{k}} Q$, and thus we can write a fully 4-dim version of the classical theorem as

$$\frac{d}{dt} \int_{\Sigma_t} Q \rho_0 u^\alpha dS_\alpha = \int_{\Sigma_t} \mathcal{L}_{\mathbf{k}} Q \rho_0 u^\alpha dS_\alpha. \quad (\text{A5})$$

A straightforward proof of Eq. A5 can be obtained if we consider $f(t) = \int_{\Sigma_t} Q \rho_0 u^\alpha dS_\alpha$. Let $\Sigma = \Sigma_0$ and $\Sigma_t = \psi_t(\Sigma)$,

where t^α is the generator of the diffeomorphism family ψ_t . Then

$$\begin{aligned} f'(0) &= \lim_{t \rightarrow 0} \frac{1}{t} \left\{ \int_{\Sigma_t} Q \rho_0 u^\alpha dS_\alpha - \int_{\Sigma} Q \rho_0 u^\alpha dS_\alpha \right\} \\ &= \lim_{t \rightarrow 0} \frac{1}{t} \left\{ \int_{\Sigma} \psi_{-t} (Q \rho_0 u^\alpha dS_\alpha) - \int_{\Sigma} Q \rho_0 u^\alpha dS_\alpha \right\} \\ &= \int_{\Sigma} \lim_{t \rightarrow 0} \frac{1}{t} \{ \psi_{-t} (Q \rho_0 u^\alpha dS_\alpha) - (Q \rho_0 u^\alpha dS_\alpha) \} \\ &= \int_{\Sigma} \mathcal{L}_t (Q \rho_0 u^\alpha dS_\alpha) = \int_{\Sigma} \mathcal{L}_t (Q \rho_0 u^t \sqrt{-g}) d^3 x \\ &= \int_{\Sigma} \mathcal{L}_{\mathbf{k}} (Q \rho_0 u^t \sqrt{-g}) d^3 x - \Omega \int_{\Sigma} \mathcal{L}_\phi (Q \rho_0 u^t \sqrt{-g}) d^3 x \\ &= \int_{\Sigma} \mathcal{L}_{\mathbf{k}} (Q \rho_0 u^t \sqrt{-g}) d^3 x - \Omega \int_{\Sigma} D_i (Q \rho_0 u^t \alpha \phi^i) dS \\ &= \int_{\Sigma} \mathcal{L}_{\mathbf{k}} (Q) \rho_0 u^\alpha dS_\alpha. \end{aligned}$$

To obtain the last line we converted the second integral in the previous line over a divergence, to a surface integral that vanishes, and also used the continuity equation in the form $\mathcal{L}_{\mathbf{k}} (\rho_0 u^t \sqrt{-g}) = 0$.

For the computation of Eq. (A2) we need to compute the third material derivatives of $x^i x^j$. We denote by $\phi^i = (\phi^A, 0)$ where capital letters take values in $\{1, 2\}$. Then $\phi^A = -\epsilon^{AB} x_B$ and the nonzero components are

$$\begin{aligned} \frac{Dx^A}{Dt} &= \Omega \phi^A := v^A \\ \frac{Dv^A}{Dt} &= -\Omega^2 x^A := a^A \\ \frac{D\alpha^A}{Dt} &= -\Omega^3 \phi^A. \end{aligned}$$

Setting $\varpi^i = (x^A, 0)$ we have

$$\begin{aligned} \dot{I}^{ij}(0) &= \Omega \int_{\Sigma} \rho_0 u^\alpha (x^i \phi^j + x^j \phi^i) dS_\alpha, \\ \ddot{I}^{ij}(0) &= -\Omega^2 \int_{\Sigma} \rho_0 u^\alpha (\varpi^i x^j - 2\phi^i \phi^j + x^i \varpi^j) dS_\alpha, \\ \dddot{I}^{ij}(0) &= -\Omega^3 \int_{\Sigma} \rho_0 u^\alpha (\phi^i x^j + 3\varpi^i \phi^j + 3\phi^i \varpi^j + x^i \phi^j) dS_\alpha. \end{aligned}$$

Using the derivatives of the multiple moments above one can compute the luminosity or the angular momentum radiated from Eq. A2. For the GW strain, assuming rotation around the z-axis, we have

$$\begin{aligned} [h_{AB}] &= \frac{2}{r} \begin{bmatrix} (\ddot{I}_{11} - \ddot{I}_{22})/2 & \ddot{I}_{12} \\ \ddot{I}_{21} & -(\ddot{I}_{11} - \ddot{I}_{22})/2 \end{bmatrix} \\ &= \begin{bmatrix} h_+ & h_\times \\ h_\times & -h_+ \end{bmatrix}. \end{aligned}$$

For the case of an exact triaxial ellipsoid the two elliptical polarization modes for head on observation along the z-axis,

we set

$$h_{(+,\times)} = \frac{4\Omega^2}{r}(I_1 - I_2)(\cos(2\Omega t), \sin(2\Omega t)), \quad (\text{A6})$$

where I_k are the principal moments of inertia. Then the emitted power and angular momentum will be,

$$|\dot{E}| = \frac{32}{5}(I_1 - I_2)^2\Omega^6, \quad (\text{A7})$$

$$|\dot{J}| = \frac{32}{5}(I_1 - I_2)^2\Omega^5. \quad (\text{A8})$$

A parameter which is often mentioned is called ellipticity of the source is defined as $\varepsilon := |I_1 - I_2|/I_3$. Although there is no rigorous counterpart in GR we can generalize as

$$\varepsilon_z := \frac{|I_{11} - I_{22}|}{I_{11} + I_{22}}. \quad (\text{A9})$$

This is the quantity that is reported in Table II.

-
- [1] B. P. Abbott, R. Abbott, T. D. Abbott, *et al.*, Phys. Rev. Lett. **116**, 061102 (2016).
- [2] <https://einsteinathome.org/>
- [3] J. Aasi *et al.*, Phys. Rev. D **87**, 042001 (2013).
- [4] M. A. Papa *et al.*, arXiv: 1608.08928.
- [5] J.D.E. Creighton and W.G. Anderson, Gravitational-Wave Physics and Astronomy: An Introduction to Theory, Experiment, and Data Analysis, Wiley-VCH, 2011.
- [6] N. Andersson, V. Ferrari, *et al.*, Gen. Rel. Grav. **43**, 409 (2011).
- [7] K. Kokkotas, Oscillations and instabilities of relativistic stars, in Gravity Astrophysics and Strings 2002, editors P.P.Fiziev and M.D. Todorov, St. Kliment Ohridski University Press, Sofia, 2003.
- [8] S. Shapiro and S. Teukolsky, Black Holes, White Dwarfs, and Neutron Stars. Wiley, New York (1983).
- [9] B. Haskell, D. I. Jones, and N. Andersson, Mon. Not. Roy. Astron. Soc. **373**, 1423 (2006).
- [10] J. L. Friedman and N. Stergioulas, Instabilities of relativistic stars General Relativity, Cosmology and Astrophysics, Fundamental Theories of Physics, Volume 177. Springer International Publishing Switzerland, 2014.
- [11] L. Baiotti and L. Rezzolla, arXiv: 1607.03540
- [12] D. Lai and S. L. Shapiro, Astrophys. J. **442**, 259 (1995).
- [13] A. L. Piro and C. D. Ott, Astrophys. J. **736**, 108 (2011).
- [14] J. L. Friedman and N. Stergioulas, "Rotating Relativistic Stars". Cambridge Monographs on Mathematical Physics. Cambridge University Press (2013)
- [15] V. Paschalidis and N. Stergioulas, arXiv: 1612.03050
- [16] T. Nozawa, Ph.D. thesis, University of Tokyo, 1997.
- [17] X. Huang, C. Markakis, N. Sugiyama, K. Uryū, Phys. Rev. D **78**, 124 (2008).
- [18] K. Uryū, A. Tsokaros, F. Galeazzi, H. Hotta, M. Sugimura, K. Taniguchi and S. I. Yoshida, Phys. Rev. D **93**, 044056 (2016).
- [19] R. A. James, Astrophys. J. **140**, 552 (1964).
- [20] S. Bonazzola, J. Frieben, and E. Gourgoulhon, Astrophys. J. **460**, 379 (1996).
- [21] S. Chandrasekhar, "Ellipsoidal Figures of Equilibrium", New Haven: Yale University Press.
- [22] S.L. Shapiro and S. Zane, Astrophys. J. **460**, 379 (1996).
- [23] S. Bonazzola, J. Frieben, and E. Gourgoulhon, Astron. Astrophys. **331**, 280 (1998).
- [24] T. Di Girolamo and M. Vietri, Astrophys. J. **581**, 519 (2002).
- [25] M. Saijo, and E. Gourgoulhon, Phys. Rev. D **74**, 084006 (2006).
- [26] D. Gondek-Rosinska, and E. Gourgoulhon, Phys. Rev. D **66**, 044021 (2002);
- [27] D. Skinner, and L. Lindblom, Astrophys. J. **461**, 920 (1996).
- [28] S. Yoshida, and Y. Eriguchi, Astrophys. J. **490**, 779 (1997).
- [29] T. W. Baumgarte, S. L. Shapiro, and M. Shibata, Astrophys. J. **528**, L29 (2000)
- [30] M. Shibata, T. W. Baumgarte, and S. L. Shapiro, Astrophys. J. **542**, 453 (2000).
- [31] L. Baiotti, R. De Pietri, G. Mario Manca, and L. Rezzolla, Phys. Rev. D **75**, 044023 (2007).
- [32] G. Mario Manca, L. Baiotti, R. De Pietri and L. Rezzolla, Class. Quantum Grav. **24**, S171 (2007).
- [33] R. De Pietri, A. Feo, L. Franci, and F. Löffler, Phys. Rev. D **90**, 024034 (2014).
- [34] F. Löffler, R. De Pietri, A. Feo, F. Maione, and L. Franci, Phys. Rev. D **91**, 064057 (2015).
- [35] M. Shibata, S. Karino and Yoshiharu Eriguchi, Mon. Not. Roy. Astron. Soc. **334**, L27 (2002).
- [36] S. Karino and Y. Eriguchi, Astrophys. J. **592**, 1119 (2003).
- [37] M. Shibata, S. Karino and Y. Eriguchi, Mon. Not. Roy. Astron. Soc. **343**, 619 (2003).
- [38] J. M. Centrella, C. B. New Kimberly, L. L. Lowe, and J. D. Brown, Astrophys. J. **550**, L193 (2001).
- [39] M. Saijo, T. W. Baumgarte, and S. L. Shapiro, Astrophys. J. **595**, 352 (2003).
- [40] C. D. Ott, S. Ou, J. E. Tohline, and A. Burrows, Astrophys. J. **625**, L119 (2005).
- [41] S. Ou and J. E. Tohline, Astrophys. J. **651**, 1068 (2006).
- [42] V. Paschalidis, W. E. East, F. Pretorius, and S. L. Shapiro, Phys. Rev. D **92**, 121502(R) (2015).
- [43] W. E. East, V. Paschalidis, and F. Pretorius, Class. Quantum Grav. **33**, 244004 (2016).
- [44] M. Shibata and S. Karino, Phys. Rev. D **70**, 084022 (2004).
- [45] N. Stergioulas, and J. L. Friedman, Astrophys. J. **492**, 301 (1998).
- [46] S. Ou, J. E. Tohline, and L. Lindblom, Astrophys. J. **617**, 490 (2004).
- [47] K. Uryū, A. Tsokaros, L. Baiotti, F. Galeazzi, N. Sugiyama, K. Taniguchi, and S. Yoshida, Phys. Rev. D **94**, 101302 (2016).
- [48] M. D. Duez, Y. T. Liu, S. L. Shapiro, and B. C. Stephens, Phys. Rev. D **69**, 104030 (2004).
- [49] A. Tsokaros and K. Uryū, Phys. Rev. D **75**, 044026 (2007).
- [50] K. Uryū and A. Tsokaros, Phys. Rev. D **85**, 064014 (2012).
- [51] K. Uryū, A. Tsokaros, and Philippe Grandclément, Phys. Rev. D **86**, 104001 (2012).
- [52] A. Tsokaros and K. Uryū, J. Eng. Math. **82**, 133 (2013).
- [53] A. Tsokaros and K. Uryū, Phys. Rev. D **91**, 104030 (2015).
- [54] A. Tsokaros, B. C. Mundim, F. Galeazzi, L. Rezzolla, and K. Uryū, Phys. Rev. D **94**, 044049 (2016).
- [55] Z. B. Etienne, J. A. Faber, Y. T. Liu, S. L. Shapiro, K. Taniguchi, and T. W. Baumgarte, Phys. Rev. D **77**, 084002 (2008).
- [56] Z. B. Etienne, Y. T. Liu, and S. L. Shapiro, Phys. Rev. D **82**, 084031 (2010)

- [57] Z. B. Etienne, V. Paschalidis, Y. T. Liu, and S. L. Shapiro, Phys. Rev. D **85**, 024013 (2012).
- [58] V. Paschalidis, Z. Etienne, Y. T. Liu and S. L. Shapiro Phys. Rev. D **83**, 064002 (2011)
- [59] V. Paschalidis, Y. T. Liu, Z. Etienne, and S. L. Shapiro Phys. Rev. D **84**, 104032 (2011)
- [60] S. Bonazzola, E. Gourgoulhon, and J. Marck, Phys. Rev. D **56**, 7740 (1997).
- [61] J. L. Friedman, K. Uryū, and M. Shibata, Phys. Rev. D **65**, 064035 (2002).
- [62] M. Shibata and T. Nakamura, Phys. Rev. D **52**, 5428 (1995).
- [63] T. W. Baumgarte and S. L. Shapiro, Phys. Rev. D **59**, 024007 (1999).
- [64] A. Harten, P. Lax, and B. van Leer, SIAM Rev. **25**, 35 (1983).
- [65] B. van Leer, J. Comput. Phys. **23**, 276 (1977).
- [66] P. Colella and P. R. Woodward, J. Comput. Phys. **54**, 174 (1984).
- [67] C. R. Evans and J. F. Hawley, Astrophys. J. **332**, 659 (1988).
- [68] J. Isenberg, Int. J. Mod. Phys. D **17**, 265 (2008); J. Isenberg and J. Nester, in *General Relativity and Gravitation*, edited by A. Held, (Plenum, New York 1980), Vol 1.
- [69] J. R. Wilson and G. J. Mathews, in *Frontiers in Numerical Relativity*, edited by C. R. Evans, L. S. Finn, and D. W. Hobill, Cambridge University Press, Cambridge, England, 1989.
- [70] T. W. Baumgarte and S. L. Shapiro, *Numerical Relativity: Solving Einsteins Equations on the Computer*, Cambridge University Press, 2010.
- [71] G. Gibbons and J. Stewart, in *Classical General Relativity*, edited by W. B. Bonnor, J. N. Islam, and M. A. H. MacCallum, Cambridge Univ. Press, 1984.
- [72] R. Beig, Phys. Lett. A **69**, 153 (1978).
- [73] E. Gourgoulhon and S. Bonazzola, Class. Quantum Grav. **11**, 443 (1994).
- [74] B. P. Abbott, R. Abbott, T. D. Abbott, *et al.*, arXiv: 1701.07709
- [75] Z. B. Etienne, V. Paschalidis, R. Haas, P. Mösta, and S. L. Shapiro Class. Quantum Grav. **32**, 175009 (2015)
- [76] Cactus Computational Toolkit, <http://www.cactuscode.org>.
- [77] J. G. Baker, J. M. Centrella, D. I. Choi, M. Koppitz, and J. R. van Meter, Phys. Rev. Lett. **96**, 111102 (2006).
- [78] M. Campanelli, C. O. Lousto, P. Marronetti, and Y. Zlochower, Phys. Rev. Lett. **96**, 111101 (2006).
- [79] I. Hinder, A. Buonanno, M. Boyle, *et al.*, Class. Quantum Grav. **31**, 025012 (2013).
- [80] M. Alcubierre, B. Brügmann, P. Diener, M. Koppitz, D. Pollney, E. Seidel, and R. Takahashi, Phys. Rev. D **67**, 084023 (2003).
- [81] Z. B. Etienne, Y. T. Liu, S. L. Shapiro, and T. W. Baumgarte, Phys. Rev. D **79**, 044024 (2009).
- [82] J. L. Friedman and B. F. Schutz, Astrophys. J. **199**, L157 (1975).
- [83] S. M. Morsink, N. Stergioulas, and S. R. Blattinig, Astrophys. J. **510**, 854 (1999).
- [84] B. D. Miller, Astrophys. J. **181**, 497 (1973).
- [85] L. Lindblom, B.J. Owen, and S. M. Morsink, Phys. Rev. Lett. **80**, 4843 (1998).
- [86] L. Lindblom and S. L. Detweiler, Astrophys. J. **211**, 565 (1977).
- [87] L. Baiotti, I. Hawke, P. J. Montero, F. Löffler, L. Rezzolla, N. Stergioulas, J. A. Font, and E. Seidel, Phys. Rev. D **71**, 024035 (2005).
- [88] B. Giacomazzo and L. Rezzolla, Class. Quantum Grav. **24**, 235 (2007).
- [89] K. Dionysopoulou, D. Alic, C. Palenzuela, L. Rezzolla, and B. Giacomazzo, Phys. Rev. D **88**, 044020 (2013).
- [90] D. Radice, L. Rezzolla, and F. Galeazzi, Class. Quantum Grav. **31**, 075012 (2014).
- [91] S. L. Shapiro, Astrophys. J. **613**, 1213 (2004).
- [92] C. W. Misner, K. S. Thorne, and J. A. Wheeler, *Gravitation*, Freeman, New York 1973.
- [93] M. Shibata and Y. Sekiguchi, Phys. Rev. D **68**, 104020 (2003).
- [94] L.S. Finn and C.R. Evans, Astrophys. J. **351**, 588 (1990).